Experimental Substantiation of Computational Thermodynamic, Kinetic, and Solidification Modeling for Cold Sprayable, Gas-atomized, Al 6061 Powder

Article · December 2020

4 authors:

Bryer Casey Sousa
Triton Systems, Inc.
75 PUBLICATIONS   **627** CITATIONS

SEE PROFILE

A. T. Nardi
VRC Metal Systems LLC
69 PUBLICATIONS   **937** CITATIONS

SEE PROFILE

Victor Kenneth Champagne Jr.
Army Research Laboratory
221 PUBLICATIONS   **4,918** CITATIONS

SEE PROFILE

Danielle L. Cote
Worcester Polytechnic Institute
85 PUBLICATIONS   **668** CITATIONS

SEE PROFILE

VIBGYOR
ePress

Experimental Substantiation of Computational Thermodynamic, Kinetic, and Solidification Modeling for Cold Sprayable, Gas-atomized, Al 6061 Powder
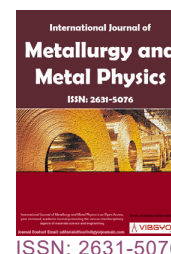
Bryer C Sousa[1]* ⓘ, Victor K Champagne Jr[2] ⓘ, Aaron T Nardi[2] and Danielle L Cote[1] ⓘ

[1]Materials Science and Engineering Program, Department of Mechanical Engineering, Worcester Polytechnic Institute, USA

[2]U.S. Army Research Laboratory, Aberdeen Proving Ground, USA

Abstract

In the majority of powder consolidation techniques, individual powder properties, such as grain size, strength, modulus, etc., are disregarded given particle melting during processing. However, in the solid-state cold spray materials consolidation process, powder particle properties significantly affect the mechanical behavior and microstructural characteristics of the consolidated material as well as the processing parameters required. Therefore, it is essential to fully characterize and derive powder properties in order to better predict the performance and behavior of cold sprayed deposits and the processing parameters needed to achieve them. An additive strength model can be used to predict the particulate strength as a function of particle diameter and solidification cooling rate. Such an additive strength model is based on thermodynamic, kinetic, and solidification principles and considers contributions to the overall particle strength by solid solution strengthening, microstructural grain size, and precipitation/dispersion strengthening, among other factors such as dislocation density and intrinsic strength. Said additive strength model quantifies the effects of the first two stages of the cold spray through-process model.

All of the stages of the through-process model for cold spray include: (1) Powder Production, (2) Powder Preparation, (3) Cold Spray Parameters, (4) Particle Impact, and (5) Post-Processing. The present paper focuses on the modeling and experimental work surrounding the Powder Production stage of the through-process model (in particular the strength contribution from the rapidly solidified microstructure). For gas-atomized Al 6061 powder, the increase in the as-atomized strength of the material due to the microstructural grain size is between 60% and 40% for 10 μm to 55 μm particles, respectively. In turn, the present paper compares theoretical predictions with experimental findings for the purpose of verification and substantiation of the computational approaches underpinning the Powder Production stage of the through-process model for cold spray. Additional consideration and analysis of the veracity of thermodynamic and kinetic modeling is also discussed. The Al 6061 cold sprayable feedstock powder chemistry led to the prediction of Mg-rich, Fe-rich, and Cu-Fe-based secondary phases, which were experimentally found to reside along the grain boundaries that were free of solute segregation.

Keywords

Cold spray, Al 6061, Through-process modeling, Gas-atomization, Rapid solidification, Computational kinetics and thermodynamics, Microstructural analysis

*Corresponding author: *Bryer C Sousa, Materials Science and Engineering Program, Department of Mechanical Engineering, Worcester Polytechnic Institute, Worcester, MA 01609, USA*

Sousa et al. Int J Metall Met Phys 2020, 5:061

ISSN: 2631-5076 | • Page 2 of 17 •
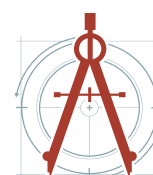
Introduction

The cold spray materials consolidation process is an important solid-state additive manufacturing method as well as repair technology for military and industrial applications because of cold spray's ability to consolidate and reclaim lightweight alloys that have high strength, durability, and toughness while also maintaining low porosity [1]. In order to maximize the benefits and broaden the variety of applications of the cold spray process, a through-process model (TPM) was developed to allow for the prediction of cold sprayed material properties as a function of the feedstock, substrate and processing parameters used. Synergy between modeling and experimental results was, and remains, crucial for developing this model and is discussed in the following sections. Moreover, while critical examination of the TPM developed for cold spray processing has been remarked upon by Sousa, et al., among others, in [2-4], the present analysis is the first explicit inspection of the computational veracity associated with the cold spray TPM through a practical experimental lens.
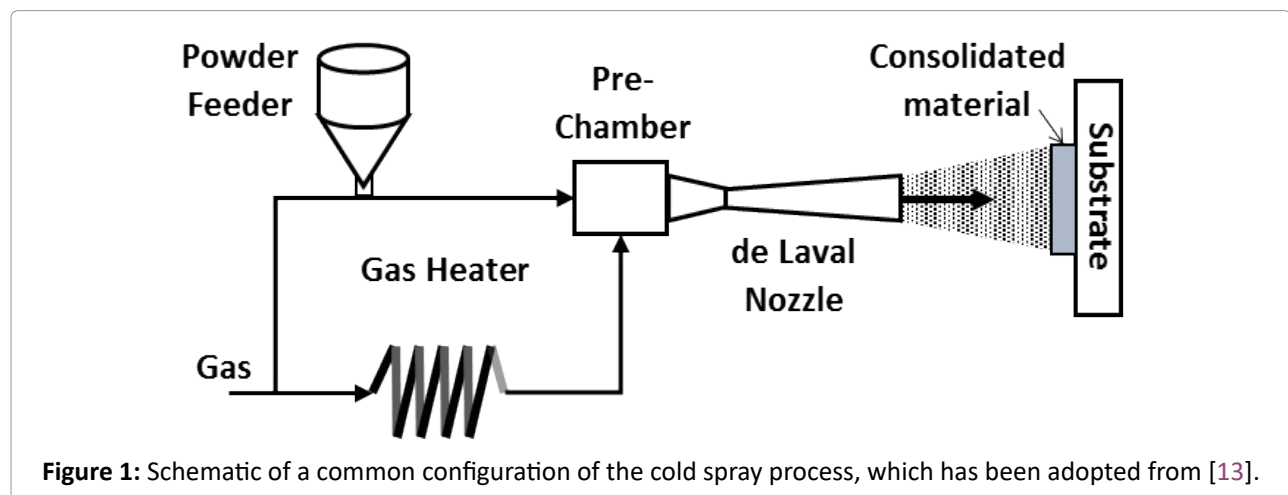
Cold spray process

The cold spray process is a material-deposition technique resulting in the consolidation of powder particles onto a suitable substrate, thus forming a coating or near net shaped part. A schematic of the process is shown in Figure 1. Powder particles, typically between 10 μm and 100 μm in diameter, are injected or introduced into a heated inert gas stream. The carrier gas and particulates are accelerated to supersonic velocities through a de Laval nozzle. The particles are then ejected fro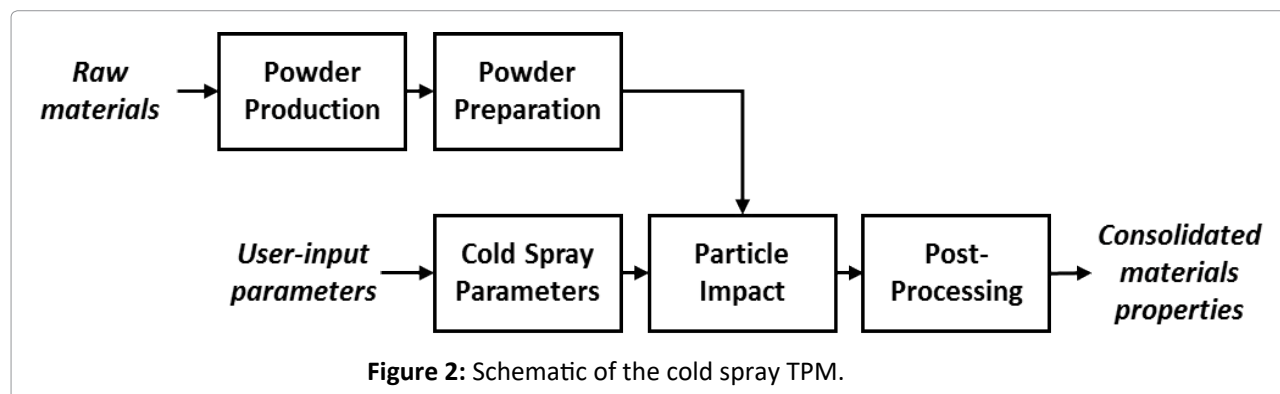m the nozzle onto a substrate at sufficiently high, supersonic, particle impact velocities such that the particles plastically deform upon impact and adhere to the substrate as long as the particle impact velocity targets the required critical impact velocity [5]. Of course, this requires one to assume a particular view of the definition surrounding the critical impact velocity, which can vary from the velocities required for 50% of the particles to bond to a target substrate, according to [6], to the variable multiplied by a coefficient of 1.3 in [7]. Nevertheless, as the cold spray materials consolidation process continues, additively deposited layers create a consolidated material layer-by-layer [1,8-10].

An important defense-based application of the cold spray process is the reclamation and repair of high-cost magnesium and aluminum aerospace parts. Examples of such applications can be found in [11]. Specifically, cold spray is used for dimensional restoration of worn or corroded parts and is accomplished by spraying directly onto a part and building up the required thickness without the concern of forming a heat affected zone, as is formed with welding and/or other thermal spray-based restoration techniques. Additionally, bulk materials and even near-net shaped parts, have been produced by the cold spray process by spraying directly onto a sacrificial mold or build plate. In fact, shaped charged liners, projectile bodies, sputter targets, and donor tubes for the explosive cladding process have been produced in this manner [12] (Figure 1 [13]).

Through-process model

With the aforementioned in mind, one may appreciate the fact that TPM's have previously been used to model other metal processing techniques,

Figure 1: Schematic of a common configuration of the cold spray process, which has been adopted from [13].

Sousa et al. Int J Metall Met Phys 2020, 5:061

ISSN: 2631-5076 | • Page 3 of 17 •

Figure 2: Schematic of the cold spray TPM.

specifically for aluminum sheet fabrication and die castings [14-17]. In order to completely model and predict the properties of the cold spray consolidations, property predictions of the feedstock powder particulates are needed, as well as the predictable effects of processing and particle-substrate impact parameters. Each of these stages were modeled independently and then integrated into a respective cold spray specific TPM framework. This holistic approach allows for the properties of the cold sprayed deposit to be predicted based on starting materials properties and processing parameters. Conversely, if there are desirable or already known mechanical property specifications needed for a given application, the TPM could be used to suggest starting materials and processing parameters to produce consolidated materials with the desired properties. The TPM for cold spray processing is represented schematically in Figure 2. The steps or stages in the top row of Figure 2 involves the matter of modeling the powder particles used as feedstock during the cold spray process. Since cold spray is a solid-state process in which a significant amount of plastic deformation and grain refinement or recrystallization can occur, and the microstructure of the feedstock powder also largely determines the microstructure in the deposit [13], one may readily find the importance of the powder-specific models underpinning the powder-related stages of the cold spray TPM as being appreciable.

The first of the two powder-based stages associated with the cold spray TPM, that is, the Powder Production stage, predicts the microstructure and mechanical properties (yield strength and hardness) of the powder particles as a function of particle diameter; specifically, for aluminum powders produced by rapid solidification via gas-atomization processing or comparable methods like that of plasma spheroidization. The Powder Prepara-

tion stage accounts for any thermal or mechanical pre-processing treatments that the particulate feedstock system undergoes following atomization and prior to being consumed during cold spray processing. The Cold Spray Parameters stage considers processing parameters such as gas temperature, gas pressure, and particulate flow rates, among others [18]. These parameters, in addition to the powder properties, are received as inputs into the Particle Impact stage. In this stage, ABAQUS/Explicit axisymmetric and three-dimensional models are used to predict system behavior upon particle impact based on processing parameters, such as impact velocity, particle temperature, and substrate temperature [3]. The final stage of the TPM is an optional Post-Processing step, considering effects of heat treatment, mechanical and/or thermochemical surface treatments on the cold spray material consolidations.

Models have been developed for powders produced by gas atomization [19-21]. Development of the cold spray process and respective particle impact models remains an ongoing matter of research and development and is included in the TPM. Modeling the pre-processing procedures associated with respective powders, as well as post-processing treatment models of cold sprayed materials are lacking. Further, there is a current disconnect among existing models of various stages shown in Figure 2. Development of these models and integration of all five modeling stages is the ultimate goal of the cold spray TPM. Therefore, recall the fact that the aim of this work is to experimentally substantiate the initial stage of the TPM for continued maturation of the final cold spray TPM.

To integrate the powder stages into the Particle Impact model, represented by the schematic in Figure 2, an additive strength model is employed.

Sousa et al. Int J Metall Met Phys 2020, 5:061

ISSN: 2631-5076 | • Page 4 of 17 •

For the present purpose, the initial additive yield strength model contributions to the overall powder particle strength as a function of particle diameter can be quantified by Eqn. 1, such that

$$\sigma_Y(d) = \sigma_o + \Delta\sigma_{ss}(d) + \Delta\sigma_{mic}(d) + \Delta\sigma_{ppt}(d), \quad (1)$$

Wherein σ_o, is the intrinsic strength of the material, $\Delta\sigma_{ss}(d)$ is the contribution from solid solution strengthening, $\Delta\sigma_{mic}(d)$ is the contribution from microstructural feature size, and $\Delta\sigma_{ppt}(d)$ is the dispersion and precipitation strengthening contribution. More recent refinements of the additive strength model have since emerged, as was described by Sousa, et al. in [2], Tsaknopoulos in [22], and inspired by the work of Thangaraju, et al. in [23], wherein

$$\sigma_Y(d) = \sigma_o + (\Delta\sigma_{ss}(d)^n + \Delta\sigma_{mic}(d)^n + \Delta\sigma_{ppt}(d)^n + \sigma_d^{\ n})^{\frac{1}{n}}, \quad (2)$$

n ranges from 1 to 2, serving as the superposition principal that aims to capture the interdependency of each term with one another at a mechanochemical level, and σ_d is the dislocation strengthening term.

As already mentioned, powder properties are especially important in modeling the solid-state cold spray process because, unlike other powder consolidation techniques where the powder particles are melted, the feedstock mechanical properties and microstructures directly influence the deposited material properties. Again, this paper focuses on the modeling and experimental work on the Powder Production stage of the TPM for cold spray processing. This stage is vital to the accurate predictions of the cold sprayed deposit properties. Specifically, the phases and microstructural grain size were computationally predicted and experimentally substantiated and explored, in part, herein.

Materials and Methods

Thermodynamic models

The first step in modeling the microstructure of the feedstock powder was to determine the equilibrium phases present. The commercially available thermodynamic software, known as Thermo-Calc (Stockholm, Sweden), was used to predict these phases using the CALPHAD ("CALculation of PHAse Diagrams") approach. This approach utilizes the minimization of Gibbs free energy to yield the most thermodynamically stable phases, which are those present under equilibrium conditions. Results are depicted in the form of isopleths, and further quantification of the isopleths can be made, producing phase fractions of equilibrium phases present as a function of temperature and composition. Pandat Software (CompuTherm, Middleton, WI, USA) was also utilized to compute respective equilibrium isopleths as well. The results of these predictive models were compared to experimental characterization using scanning electron microscopy (SEM), transmission electron microscopy (TEM), and energy dispersive spectroscopy (EDS), and recently reported experimental findings, as discussed in the Thermodynamic Model Results section.

Solidification model

Due to the small size and therefore extremely rapid solidification rates of the gas-atomized powder particles under consideration, standard solidification models were not used. Particle cooling rate has a significant effect on the microstructure of the powder particles [24]. This subsequently determines the material and mechanical properties of the powder particles and is therefore important as input into kinetic models, discussed below, which consider time-dependency. A rudimentary model to determine the cooling rate of the powder particles during formation via gas atomization was created. The majority of alloyed aluminum powders used in the cold spray processing research reported in the literature to date were produced by the gas atomization process, including the powders studied in this work. In gas atomization, a metal melt contacts a high velocity gas stream resulting in the breakup of the melt into small particles. The particles solidify as they travel through the atomization chamber and are collected as solidified powder particles [25].

A simplified heat transfer model for powder particle solidification during the gas atomization process was presented by He, et al. in [26] by way of making the assumptions of Newtonian heat flow and neglecting the negligible heat loss to radiation and internal conduction. The Biot number for the powder particles was calculated for various diameters and were all << 0.1, validating the assumption of negligible internal thermal conduction. The resulting equation is formed upon the assumption that the relative velocity between molten particu-

Sousa et al. Int J Metall Met Phys 2020, 5:061

ISSN: 2631-5076 | • Page 5 of 17 •

lates and the atomizing gas approaches zero, such that

$$\left| \frac{dT_d}{dt} \right| = \frac{12}{\rho C_p}(T_d - T_g)\frac{K_g}{d^2}, \quad (3)$$

Wherein C_p is the specific heat of the droplet, T_d is the droplet temperature, T_g is the gas-atomizing temperature, ρ is the droplet density, k_g is the thermal conductivity of the gas, and d is the droplet diameter. Regarding the determination of the thermophysical properties for Equation 3, the molten droplet properties were calculated using JMatPro software (Sente Software Ltd.) as a function of temperature. The thermal conductivity of the argon gas was generated using GRANTA CES EduPack software (ANSYS, Inc.). Note that the powder studied computationally and experimentally herein may have been produced using another inert atomization gas. However, given the recent publication of similar results by Sousa, et al. wherein a nitrogen atomization gas was utilized [27], argon was identified as another gaseous medium of relevance and interest.

The relationship between secondary dendrite arm spacing, which acts as an effective grain size, and cooling rate has been established by the following equation, and has been experimentally verified for numerous alloy systems, referenced in [19], such that

$$\lambda_2 = \lambda_0 \left(\frac{dT_d}{dt} \right)^{-n}, \quad (4)$$

Where λ_2 is the secondary dendrite arm spacing, λ_0 and n are alloy system-dependent constants, T is the droplet temperature, t is time; $(dT_d)/dt$ is therefore the cooling rate of the droplet. In the case of powder particles, the microstructure may yield grains, cellular units, dendrites, or an amorphous structure depending on composition, particle size, and cooling rate. In this work, and in Equation 4, the secondary dendrite arm spacing refers to dendritic low-angled grains. λ_2 as a function of initial cooling rate of the melt data was available from JMatPro. Data for Al 6061 was plotted and fit to a power law curve to determine the constants λ_0 and n to be 100.99 and 0.33, respectively. That being said, one should appreciate the fact that this approach does not necessarily account for undercooling and the like during rapid solidification. Nevertheless, it still provides researchers with a baseline that has been shown to have merit elsewhere [2,27].

With this data, λ_2 can be experimentally mea-

sured in particles that contain and exhibit microstructural grains to experimentally calculate cooling rates. Not all particles, however, form these microstructural features. As previously mentioned, particles that solidify at very rapid cooling rates can form amorphous particles, also noted by [19,20,28]. Since the particle cooling rate is directly proportional to the respective particle size, wherein smaller particles generally cool more rapidly, the smallest particles are those which have the greatest likelihood of forming amorphously. Dendritic microstructures only form when relatively less rapid cooling rates are incurred (i.e., slower than the cooling rates affiliated with the amorphous particles), and after a recalescence stage. These are the particles for which λ_2 can be measured, and these "less rapid" cooling rates can be estimated.

As previously mentioned, the cooling rate of each powder particle affects its resulting microstructure. Finer microstructural sizes result from more rapidly cooling particles. Since cooling rate is a direct function of powder size, the microstructural feature size also varies with powder particle size, though the dependency of microstructural feature size is stronger on cooling rate than powder size due to varying degrees of undercooling present [25]. Despite the variation in undercooling between particles of equal size adding a degree of variability in actual cooling rate and powder particle size, there is still a strong relationship between powder particle size and microstructural effective grain size.

Combining Equations 3 and 4, an equation for the secondary dendrite arm spacing or the effective microstructural grain size (λ) as a function of powder particle size can be determined, as shown in Eqn. 5,

$$\lambda = \lambda_0 \left(\frac{12}{\rho C_p}(T_d - T_f)\frac{k_g}{d^2} \right)^{-n}. \quad (5)$$

To quantify the contribution of this effective microstructural grain size to the strength of the powder particles from Equation 1, the Hall-Petch relationship is used, wherein

$$\Delta\sigma_{mic}(d) = k\lambda^{-0.5}, \quad (6)$$

Where σ_o and σ_o are the yield strength and intrinsic yield strength of the material, respectively, and k is a material constant. The relationship of effective microstructural grain size, powder particle size, and cooling rate is verified experimentally in

Sousa et al. Int J Metall Met Phys 2020, 5:061

ISSN: 2631-5076 | • Page 6 of 17 •

the Solidification Model Results section. The additional additive yield strength contribution terms in Equation 1, which includes solid solution strengthening and precipitation/dispersion strengthening, are generally calculated after the Powder Preparation stage, wherein phases and properties are controlled via thermal pre-processing of powder prior to use in cold spray and are therefore not quantified in this paper. That being said, secondary intermetallic phases are considered for the as-solidified gas-atomized Al 6061 under consideration as will be discussed further hereafter.

Computational kinetic models

If the Scheil module or framework is not employed during thermodynamic modeling, the thermodynamic models presented earlier predict equilibrium conditions, which do not likely fully represent the phases present in the powder particles upon solidification due to the particles extremely high cooling rates, as discussed in the previous section. Therefore, kinetic consideration must be concurrently presented. Sente Software's JMat-Pro and Thermo-Calc's software's TC-PRISMA and
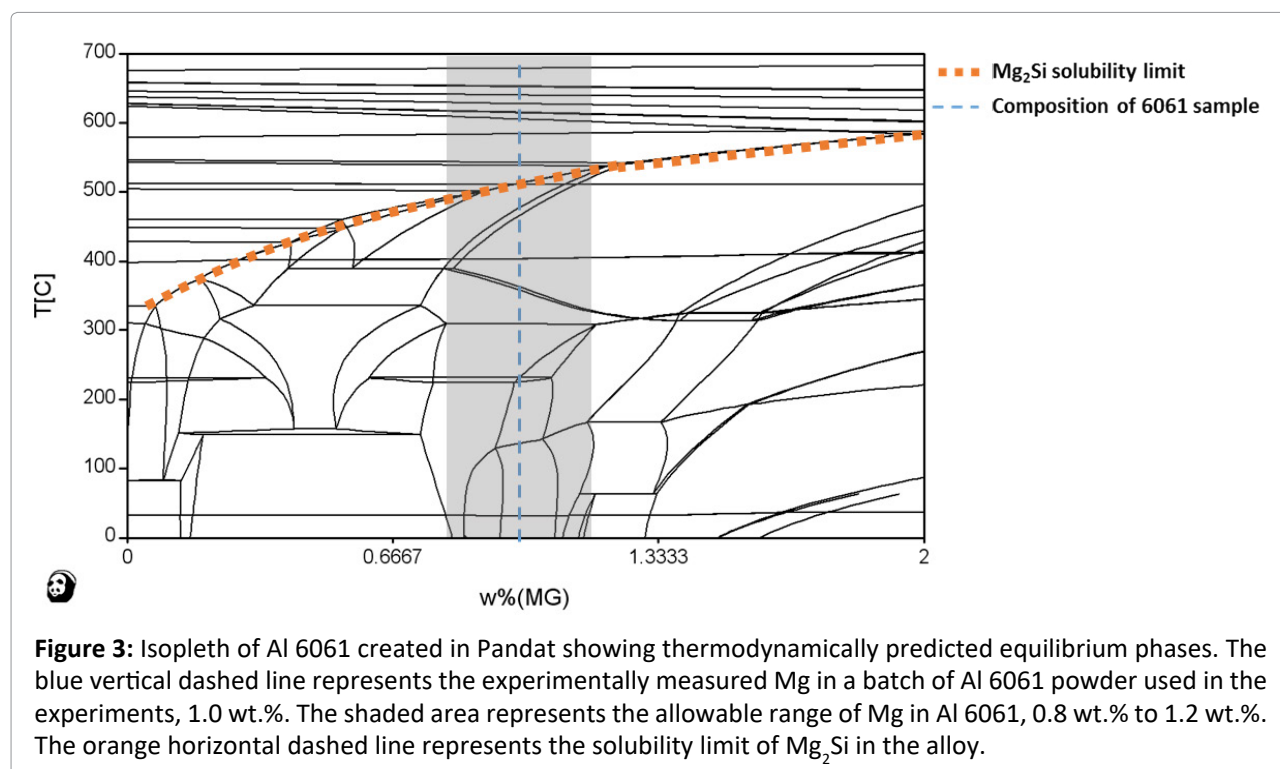
DICTRA were used to perform basic kinetic calculations, and are widely used in the field [29,30]. Calculations include the fraction of secondary phases formed during solidification, which can be displayed as continuous cooling transformation (CCT) curves. However, as will be shown shortly hereafter, the CCT curves for Mg_2Si in the gas-atomized metallurgical system being modeled partly deviated from experimental analysis.

Experimental

Gas-atomized and pre-alloyed Al 6061 powder was experimentally characterized in order to verify results from the aforementioned predictive models. The composition is shown in Table 1 was determined by direct current plasma emission spectroscopy. A thin foil from an approximately 20 μm size powder particle was prepared by a FEI 200 TEM focused ion beam (FIB) and viewed in an FEI Technai F30 transmission electron microscope. EDAX Sapphire EDS with a Si(Li) detector was used to verify the composition of phases observed in the microstructure. A sampling of loose powder was mounted onto copper tape, dipped into a 0.5% hydroflu-

Table 1: Specific composition of gas-atomized Al 6061 powder studied herein.

Element	Al	Mg	Si	Fe	Cu	Cr	Zn	Mn	Ti
Weight %	97.3	1.000	0.600	0.350	0.275	0.195	0.125	0.075	0.075

Figure 3: Isopleth of Al 6061 created in Pandat showing thermodynamically predicted equilibrium phases. The blue vertical dashed line represents the experimentally measured Mg in a batch of Al 6061 powder used in the experiments, 1.0 wt.%. The shaded area represents the allowable range of Mg in Al 6061, 0.8 wt.% to 1.2 wt.%. The orange horizontal dashed line represents the solubility limit of Mg_2Si in the alloy.

Sousa et al. Int J Metall Met Phys 2020, 5:061
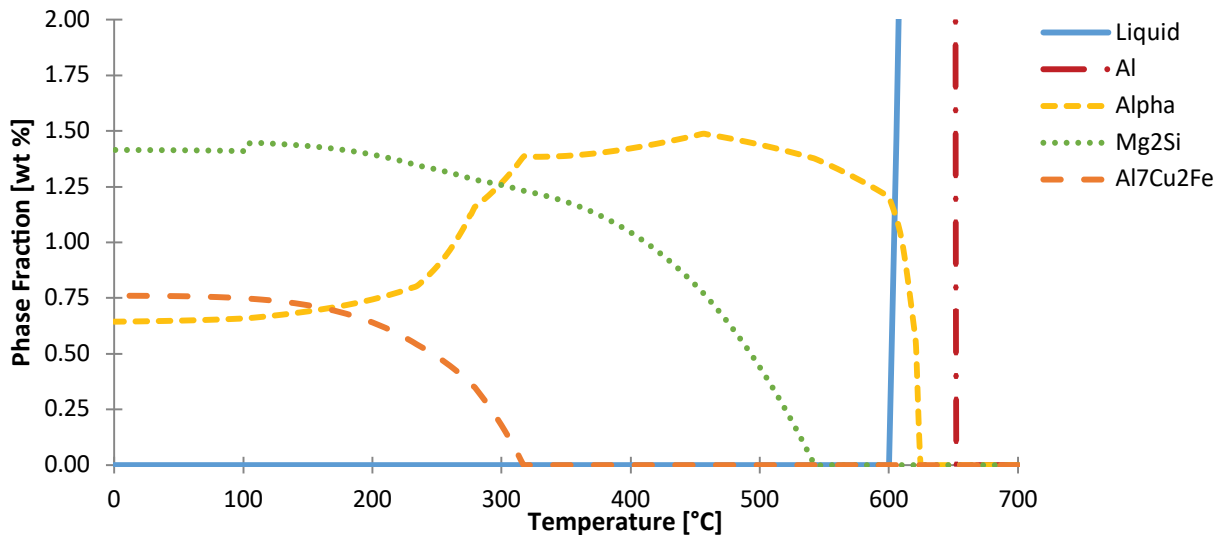
ISSN: 2631-5076 | • Page 7 of 17 •

Figure 4: Equilibrium phase fractions in Al 6061 as a function of temperature at the composition given by the blue vertical dashed line from Figure 3 (1.0 wt% Mg). Phases with phase fractions not exceeding 0.25 wt% are not shown.

oric acid and distilled water solution and viewed in a JSM-7000FX SEM to allow for measurements of particle and microstructural feature size.

Results

Thermodynamic models

An isopleth of Al 6061 is shown in Figure 3. Due to the large number of equilibrium phases present, the phase names are not shown on the isopleth in this paper, but each line represents a phase boundary. The blue dashed vertical line at 1.0 wt% Mg represents the amount of magnesium in the Al 6061 sample, given in Table 1. The shaded region in Figure 3 between 0.8 wt% Mg and 1.2 wt% Mg represents the allowable range of Mg in Al 6061 according to standardized U.S. military specification. It was noted that despite an alloying having a composition within the specification range, several different phases may actually be present, depending on the composition of the particular batch of alloys received. Finally, the orange horizontal dashed line represents the solubility limit of Mg_2Si in the alloy as a function of the wt.% Mg present and temperature.

Using the same thermodynamic principles, diagrams showing equilibrium phase fractions as a function of temperature were created for Al 6061, as shown in Figure 4. An FCC matrix is the primary phase and is out of viewing range over the majority of the temperature range due to the scale of the
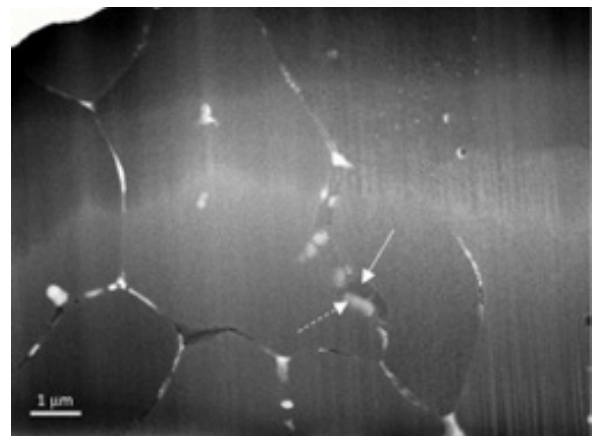

Figure 5: STEM micrograph of a gas atomized Al 6061 powder particle showing different precipitates that have formed along the grain boundaries during solidification.

diagram. The major secondary phases predicted are Mg_2Si, Al_7Cu_2Fe, and alpha ($Al_{47}(Fe,Mn,Cr)_{11}Si_5$ or Al_8Fe_2Si), which is not to be confused with the FCC matrix Al, since the FCC matrix is often reported using the Greek symbol for alpha in aluminum systems too.

A scanning TEM micrograph of an Al 6061 powder particle is shown in Figure 5. Individual grains within the powder particle are observed, which are outlined by precipitates at the grain boundaries. Three secondary phases were found and analyzed by XEDS. The darkest phase contained Mg

and Si, represented by the solid arrow in Figure 5. The white and light gray phases were Fe-containing, indicated by the dashed arrows. This was consistent with analysis presented in [27]. These phases correspond to the major secondary phases that are predicted by the thermodynamic models, shown in Figure 4: Mg_2Si and Fe-containing phases, α (Al_{47}(Fe,Mn,Cr)$_{11}Si_5$ or Al_8Fe_2Si) and Al_7Cu_2Fe. The composition from XEDS of the Fe-containing phases does not perfectly correlate with the stoichiometry predicted by the thermodynamic models. Additional analysis of the Mg_2Si phase revealed a 2:1 Mg:Si stoichiometry without the equilibrium Mg_2Si crystal structure. This work will be presented separately; however, one can explain this slight stoichiometric deviation by way of considering the fact that the phases present in the gas-atomized powder are likely meta-stable versions of the phases formed by the rapid cooling rate. This verified the need for the time-dependent kinetic models.

Solidification models

In this work, Al 6061 particles between 10 μm and 50 μm diameters were studied. Using Equation 3, depicted in Figure 6, cooling rates between 1.0 × 10^6 °C/s and 3.5 × 10^4 °C/s were predicted. These rates are in good agreement with gas atomization cooling rate predictions made elsewhere [27]. The rates are also consistent with similar additional research that considered the gas atomization-based solidification of aluminum alloys and pure copper particulates in [2,4].

The etched powder described in the Materials and Methods section of the present manuscript was viewed in an SEM in order to verify the results of the solidification model. Based on the powder particle size of the feedstock shown in Figure 7, cooling rates were calculated using Equation 3, as shown in Figure 6. The individual powder particles are shown along the calculated cooling rate gradient. The experimentally calculated cooling rates agree with predicted cooling rates for gas atomized particles [19,20,28]. As the experimentally calculated cooling rate increases to the left of the curve in Figure 6, and to the left region in Figure 7, the microstructural secondary dendrite arm spacing-based effective grain size decreases until amorphous powder particles are observed at very high cooling rates.

Equation 5 of the solidification model was substantiated quantitatively by experimentally measuring the effective microstructural grain size and particle size. Figure 8 shows the comparison between the theoretical cooling rate calculations and the experimental results for Al 6061. Note that the assumption of an argon-atomization gas as the atomizing gaseous media of relevance for
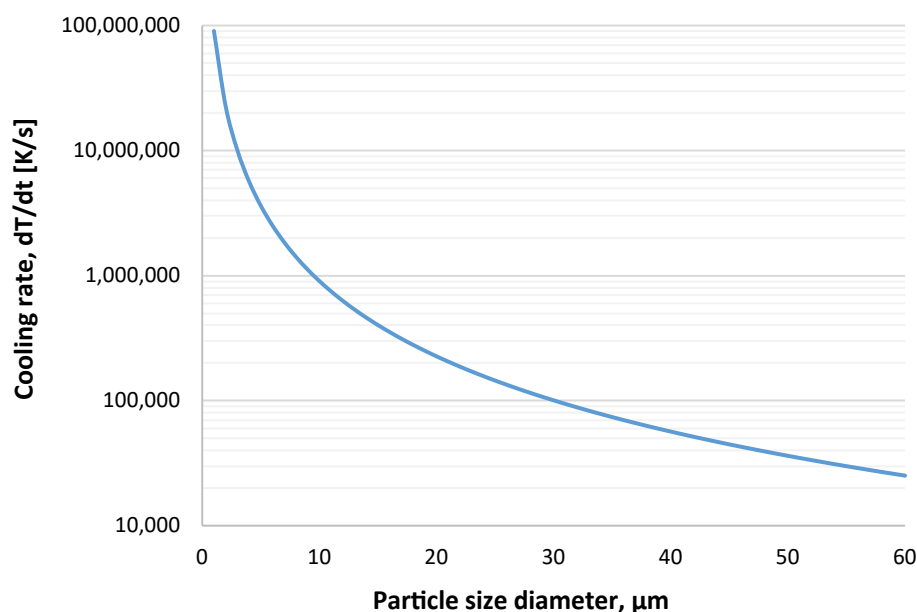

Figure 6: Cooling rate curve as a function of particle diameter resulting from the simplified solidification model given by Equation 3 for Al 6061 in an argon atomizing gas.
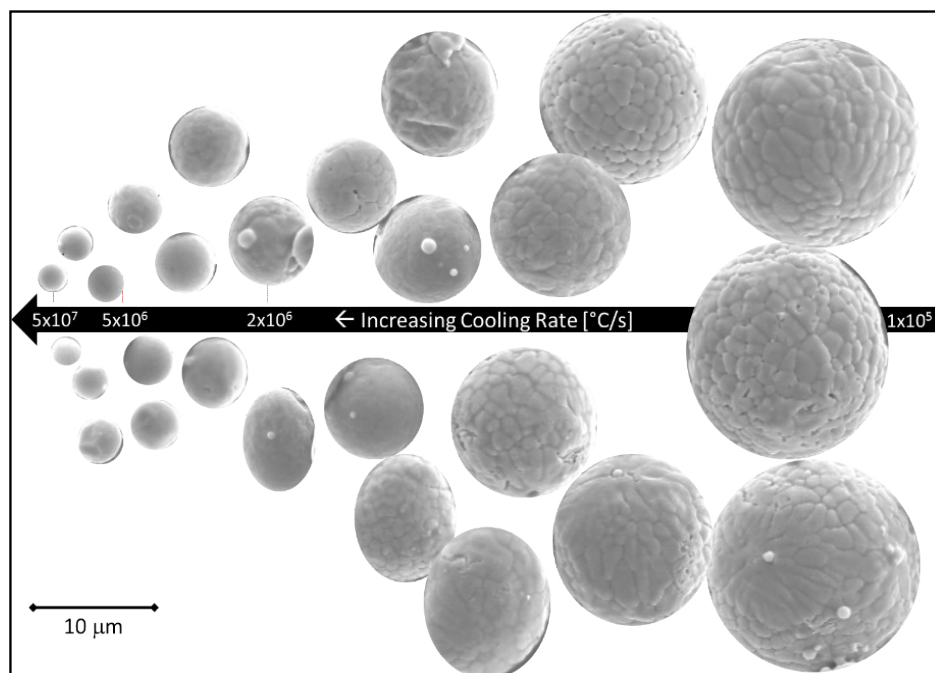
Figure 7: SEM analysis of etched Al 6061 powder particles, which visually shows the relationship between particle size, effective microstructural grain size, and cooling rate. In the relatively larger particles captured in this figure, dendritic outer microstructures are observable alongside the amorphous micrometric spheres captured as well.
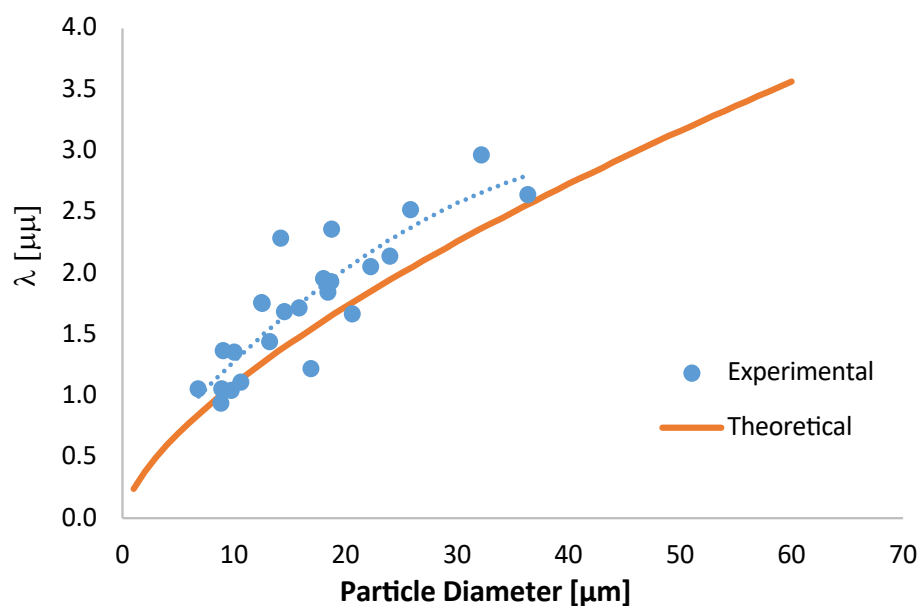

Figure 8: Theoretical and experimental relationship between the effective grain size and powder particle diameter when the solidification-based cooling rate calculations assumed the use of argon as the atomizing gaseous medium.

modeling purposes may have caused the discrepancy between the theoretical and experimental λ versus particles diameter curves found in Figure 8.

For example, if a diatomic atomization gas was utilized, then the internal energy of the atomizing gas and ability to transfer energy away from the rap-

Sousa et al. Int J Metall Met Phys 2020, 5:061

ISSN: 2631-5076 |• Page 10 of 17 •

idly solidifying material at the molecular level will be defined according to vibrational, rotational and translational kinetic energy terms versus the solely translational kinetic energy term affiliated with monoatomic gases like that of Ar. Continued discussion and analysis of the results presented in Figure 8 are presented in the subsequent Discussion section of the present article.

Additionally, experimental verification and analysis via etched powder particle effective grain size measurements may have introduced over etching-based measurements to be recorded, which would have deleteriously impacted image analysis quantification of the microstructural grain sizes. Nevertheless, the agreement between the calculated λ vs. particle diameter curve, in contrast with the experimental data curve in Figure 8, demonstrates the underlying appropriateness of the computational/theoretical approach taken for the Powder Production stage of the cold spray TPM. The present work was found to be agreeable with recent works too [2,27]. In any case, the increase of strength of the powder particles due to the contribution of microstructural grain size was calculated by way of the Hall-Petch relationship that was given in Equation 6. This was graphically represented in Figure 9. This contribution is included in the second term of the additive strength model defined in Equation 1.

Kinetic models

Figure 10 contains continuous cooling transfor-

mation (CCT) curves for the formation of Mg_2Si in Al 6061, which was created using JMatPro. Solidification models, as discussed in the Solidification Models subsection of the Results, approximated the cooling rate of the majority of Al 6061 powder particles used in the cold spray process to be between 3.5×10^4 °C/s to 1×10^6 °C/s. According to the CCT curves for the equilibrium Mg_2Si phase, the stable equilibrium form of the phase would not crystallize during solidification of these powders. However, cooling rate depends on powder particle size and undercooling too. Larger powder particles typically have a slower cooling rate, resulting in the formation of additional phases and a higher amount of these phases. This result is not evident when only observing the equilibrium isopleths and shows the necessity of kinetic considerations.

Discussion

This paper focused on the modeling and experimental verification on the Powder Production stage of the TPM for cold spray applications. Specifically, the phases and microstructural grain sizes were computationally derived, and the computational results were experimentally verified and substantiated to ensure that future advancements of the cold spray TPM will continue more readily. This data is an important and necessary input for the subsequent stages of the TPM. The equilibrium isopleth given in Figure 3 can be used to observe the variation in phases formed as a function of al-
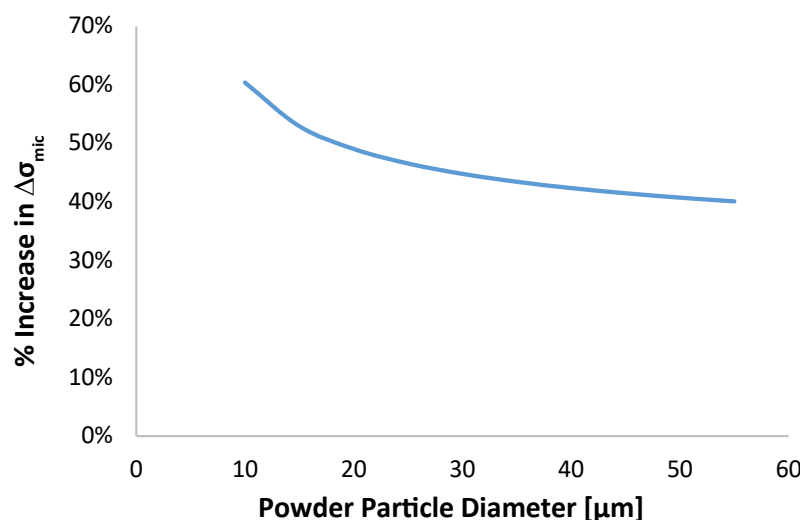

Figure 9: The increase in the strength predictions, relative to the intrinsic material strength, of the powder particles due to the microstructural grain size, as calculated via the Hall-Petch relationship expressed in Equation 6.
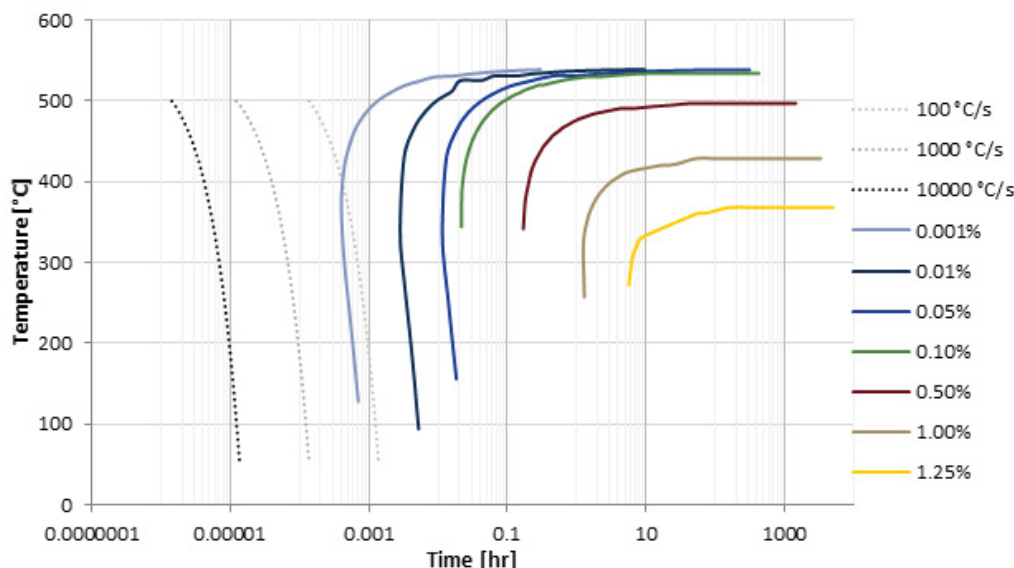
Sousa et al. Int J Metall Met Phys 2020, 5:061

ISSN: 2631-5076 |• Page 11 of 17 •

Figure 10: CCT curves for the formation of stable Mg₂Si in Al 6061 given in mass percent of the predicted equilibrium amount. Powder solidification models for the powders used in this study show cooling rates around 1×10^4 °C/s to 1×10^5 °C/s, which would result in no stable Mg2Si phase forming during solidification (as shown via STEM analysis, and will be discussed in the subsequent section shortly hereafter, non-equilibrium, metastable Mg2Si intermetallic crystal structures were observed experimentally nonetheless).

teration in chemical composition (even when the same nominal alloy designation is under consideration). The data from Figure 3 reveals the potential variation in equilibrium phases present in different samples of the same material despite all being within the allowable specification range of composition, as indicated by the shaded region of the isopleth. Also, composition of the alloy can be varied to produce desired phases or avoid deleterious secondary phases. Finally, these isopleths can be used to determine the alloy's potential for precipitation hardening as well.

These isopleths are used to determine initial predictions of phases present in the Al 6061 gas-atomized alloy under investigation. The thermodynamically predicted phases in Al 6061 in Figure 4 were qualitatively consistent with the experimental TEM analysis of the powder. Nevertheless, kinetic consideration was still given. While thermodynamic models can be very accurate for traditional cast alloys, the extremely high cooling rates predicted by Equation 2, and plotted in Figure 6, likely do not allow the traditionally equilibrium phases to form during the solidification of the powder particles via gas atomization. This is evident in the cooling curves in Figure 10, where the cooling rates of the powder particles used in cold spray are between

3×10^4 °C/s to 1×10^6 °C/s. These rates are even higher, or further to the left, of the plotted cooling rates, indicating that they will never intersect the stable Mg₂Si cooling curves, t therefore this phase, in an equilibrium and stable state, is absent in the as-atomized powder. That said, non-equilibrium, metastable Mg₂Si intermetallics were experimentally recorded and identified, highlighting Mg₂Si's non-stable presence within the feedstock studied.

Phases predicted by the thermodynamic and kinetic models contribute to the initial strength of the cold sprayable powder particles. Depending on the coherency of the predicted secondary phases with the matrix phase, various yield strength models are used calculate the resultant strength contribution from the presence of precipitates. This is captured by the last term in the additive strength model in Equation 1 and one of the terms in Eqn. 2. At the same time, Figure 8 shows the relationship between the effective microstructural grain size and powder particle diameter for Al 6061, which was given by Equation 5. The experimental results show good agreement with the predicted values. However, the agreement was not as pronounced as those demonstrated by Sousa, et al. in [2,27] recently. This may have been due to the fact that knowledge of the atomizing gas species utilized

in Sousa, et al.'s research enabled more accurate calculations. As will be mentioned in the Conclusion section, the use of etched particle exteriors for grain size measurements herein, rather than cross-sectionally etched particulate specimens may have also contributed to the less agreeable nature of the experimental analysis with the cooling rate calculations. This data is important in determining the mechanical properties of the powder particles since the microstructural grain size has a direct correlation with material strength, as given by the Hall-Petch relationship that was expressed in Equation 6.

This microstructural strength contribution depends on particle diameter since smaller particles generally have finer microstructural grain sizes, which in turn increases the Hall-Petch strength contribution term as shown in Figure 9. For Al 6061 it is predicted that cold sprayed particles within the range of 10 μm to 55 μm contribute an additional 60% to 40% of the material intrinsic strength to the powder particles' intrinsic as-received strength, respectively. The data for the additive strength model is used as a starting point for the model integration, combined with the next stage of the TPM, Powder Preparation, and employed as input into the Particle Impact TPM stage. Effects of heat treatment, degassing, etc., alter the results from the first stage and are considered in the Powder Preparation stage, which has partially been addressed elsewhere and will be presented in future work.

Regarding the way in which the present research and findings compare and contrast with the rest of the readily identified scientific literature surrounding rapidly solidified, gas-atomized, cold sprayable Al 6061, one may consider a few works of immediate relevance. Specifically, in 2019, Tsaknopoulos, et al. utilized computational approaches and microscopy to better understand the phases present in gas-atomized Al 6061 powder too [31]. Interestingly, Tsaknopoulos, et al.'s Al 6061 feedstock composition was varied in comparison with the wt.%'s recorded in Table 1 herein, resulting in a difference between the specific phases predicted and identified in [31] and those presented during the course of the present research. Specifically, Tsaknopoulos, et al.'s gas-atomized Al 6061 had 5% less Mg, approximately 18% less Si, 22.86% less Fe, approximately 9.1% less Cu, approximately 55.38% less Cr, 72% less Zn, approximately 55% less Mn,

and 68% less Ti, versus the powder characterized during the course of the present research.

Considering the resultant phases predicted and discussed by Tsaknopoulos, et al. in contrast with those discussed in the Results section of the present work, one ought to note that the Al 6061 feedstock chemically analyzed herein was not mechanically sieved to a size category of 38 μm to 45 μm, which was the case in [31]. Given the fact that previous research has shown that chemical composition can vary as function of gas-atomized powder size characteristics, the composition in Table 1 may be more representative of the respective batch of feedstock considered while the chemistry recorded in [31] is less representative of the total average and more representative of the 38 μm to 45 μm category only. To substantiate this possibility, one may consider the work of Pettersson wherein the chemical composition of a gas-atomized Ni-based alloy powder was found to vary in terms of Cr, Si and Fe content when the powder's respective D50's varied from 111.03 μm to 103.05 μm, for example [32].

Returning to the variable resultant phases predicted and hypothesized herein and those discussed by Tsaknopoulos, et al. elsewhere for the same nominal gas-atomized Al 6061 feedstock, as well as the varied chemistry between the two particulate systems, it stands to reason that neither party was incorrect. Instead, if we consider phase formation and the respective chemical sensitivities of formable phases to the vast difference in Si, Fe, Cr, Zn, Mn, and even Cu wt.%'s between the two gas-atomized systems being compared, one could surmise that phases would be more or less likely to nucleate during solidification. In fact, one could further analyze the respective alloying elemental ratios in conjunction with the resultant phases too, since ratios of various alloying elements with one another are known to promote the precipitation of certain intermetallics. Accordingly, the fact that $Al_9Fe_2Si_2$, T-phase ($Al_2Mg_3Zn_3$ or $(Al,Cu,Zn)_{49}Mg_{32}$), and Mg_2Si were identified by Tsaknopoulos, et al. as the three most abundant phases predicted via computational thermodynamics in [31] may follow from the varied chemistry relative to the compositions recorded in Table 1 above.

Beyond the discussion surrounding the enhanced sensitivity of secondary phase formation (in the gas-atomized Al 6061 studied herein) to

Sousa et al. Int J Metall Met Phys 2020, 5:061

ISSN: 2631-5076 |• Page 13 of 17 •

compositional chemistry of a nominal alloy system, one may also consider matters of solidification microstructure (i.e., cellular, dendritic, equiaxed, dendritically cellular, etc.) and the topic of chemical segregation in the gas-atomized Al 6061 particulates. To begin, the matter of chemical segregation was considered prior to solidification microstructures. That said, one may recall that Tsaknopoulos, et al., in [31], identified multiple studies wherein Rokni, et al. claimed to have observed solute segregation in gas-atomized aluminum powders (see [33], for example). Unsurprisingly, Rokni, et al. wasn't alone; rather, Sabard, et al. claimed to have observed a noteworthy amount of chemical segregation in gas-atomized Al-based alloyed and cold sprayable feedstock too [34]. However, closer inspection of the literature, in conjunction with the present findings, suggests that internal chemical segregation of alloying elements within gas-atomized Al-based alloys is intimately dependent upon powder production parameters, cooling rates, and composition too.

From the above, one may appreciate the non-universality of chemical segregation within gas-atomized alloyed aluminum microparticles. For instance, in gas-atomized Al 5056, Tsaknopoulos, et al. observed Mg-segregation between the grain boundary regions and a supersaturated aluminum matrix in [35]. But for the Al 6061 shown in Tsaknopoulos, et al.'s earlier work, elemental TEM-HAADF EDS maps revealed discrete precipitates/dispersoids along the grain boundaries in regions that were apparently free of solute segregation. This was also apparently the case when researchers from the same institution as Tsaknopoulos, et al. studied Al 2024 and Al 7075 in a similar matter when the feedstock was once again gas-atomized [36,37]. Interestingly, the explanation for the lack of solute segregation in the Al 2024 was articulated by Walde, et al., wherein the authors state the following: "During rapid solidification, there is solute microsegregation of the alloying elements at the boundaries. This segregation is highly unstable with a high propensity for the formation of secondary phases. Thus, the S-phase and Al_2Cu form rapidly, while the Fe and Mn have no time to diffuse. Based on the literature data compiled in the Thermo-Calc databases, it is known that Fe and Mn are soluble in Al_2Cu..." [36].

Consequently, this certainly calls into question

the overarching and commonly accepted stance that chemical or solute segregation (internally and not at the surface) is generally present in alloyed aluminum feedstock for cold spray that was manufactured via rapid solidification pathways. Notably, Tsaknopoulos, et al. and Walde, et al. are not the only researchers who have directly or indirectly captured data for non-Al 5056 gas-atomized particulates with supersaturated matrix phase states and secondary phases in place of chemical segregation in the atomized material. The STEM EDS performed by Evans, et al. upon rapidly solidified Al 6061 feedstock was consistent with the segregation-less and saturated state in [38]. Similarly, Bedard, et al. also noted that an Al 6061 gas-atomized feedstock in the as-atomized state was comprised of Mg-Si and Fe-Si-Al phases rather than chemical segregation due to the solidification conditions [39], which was therefore rationalized in a manner that was similar to that detailed for gas-atomized Al 2024 in the passage above. Moreover, Vijayan, et al.'s in-situ STEM-HAADF EDS analysis of gas-atomized Al 6061 and Al 5056 was consistent with the trends just detailed [40].

Stated otherwise, Vijayan, et al. found that chemical segregation of Mg was present in Al 5056, but Al 6061 appeared to be remarkably free of solute segregation, especially Mn and Cr for their Al 6061 system. At the same time, Vijayan, et al. also identified not only Mg-rich and Fe-rich phases along boundaries, but also Cu-rich phases, all of which is consistent with the equilibrium phase fractions of Mg_2Si (Mg-rich), Al_8Fe_2Si or alpha (Fe-rich) and Al_7Cu_2Fe (Cu-rich) calculated and represented in Figure 4 for the present Al 6061 system considered herein. It is also worth mentioning the reported observations surrounding a gas-atomized Al-Cr-Mn-Co-Zr nanocomposite powder that was studied in [40] too, wherein there was also "no evidence for segregation."

Having now discussed the likely lack of chemical segregation within the Al 6061 powders internal microstructure studied herein, we may consider the matter of solidification structure (dendritic, equiaxed, cellular, etc.) after first addressing the matter of chemical segregation near the powders surface. More to the point, the aforementioned discussion surrounding chemical segregation was limited to the inner region of the rapidly solidified, gas-atomized, Al 6061 system, which is not the case when

Sousa et al. Int J Metall Met Phys 2020, 5:061

ISSN: 2631-5076 |• Page 14 of 17 •

surface segregation at the outer surface is considered. As such, Ernst, et al. recently demonstrated the fact that the unique surface oxide/hydroxide state of Al 6061 microparticles can be "explained on the basis of Mg surface segregation during the gas-atomization process" in [41]. Nevertheless, such surface segregation is limited to the outer nano-scale surface for Al 6061 and not the internal solute distribution, which was just considered.

As for the microstructural solidification state of rapidly solidified, gas-atomized, Al-based alloys, many have stated that microparticles have a cellular polycrystalline structure. For instance, Leazer, et al. stated that their Al-Cu binary "powders show a nearly smooth surface with depression at the cell boundaries clearly displaying cellular solidification. Cellular solidification is a product of gas atomization as the particles experience a very high cooling rate, ~11,000 K/s, that does not allow for the growth of dendritic arms" in [42]. However, as noted by Nastic, et al. in 2020 [6], "the droplets will experience rapid cooling and solidification... and result in a microstructure with fine, ultrafine, or even dendritic grains," which is in stark contrast with the assertion by Leazer that cellular solidification is declaratively linked to gas-atomization. Commendably, Nastic, et al. pointed to the work of Duflos, et al. from 1982 which found equiaxed and dendritic microstructures in alloyed gas-atomized metallic systems as a function of solidification quench rates [43]. The identification of equiaxed grains in metallic powders processed via gas-atomization methods is also consistent with [44], among others.

Conclusion

During the course of this research, thermodynamic, solidification and kinetic modeling of rapidly solidified gas-atomized Al 6061 powder was considered. The computational analysis of said cold sprayable feedstock powder was coupled with experimental analysis to explore the veracity of the in-silico approach taken herein for the powder production stage of the TPM for cold spray processing. Accordingly, the following concluding remarks are itemized and presented below, followed by a consideration of future work.

1. The equilibrium isopleths procured by way of Pandat and Thermo-Calc for the chemical composition obtained via direct current plasma emission spectroscopy revealed the major secondary equilibrium phases, within the gas-atomized Al 6061 system considered herein, as being Mg_2Si, Al_7Cu_2Fe, and alpha, given as $Al_{47}(Fe,Mn,Cr)_{11}Si_5$ or Al_8Fe_2Si.

2. While the rapid solidification conditions of the gas-atomized Al 6061 achieve a highly non-equilibrium, supersaturated and metastable microstructural character, STEM XEDS revealed three secondary phases experimentally as well. The microscopy-based analysis and phase characterization of the three intermetallics identified were consistent with the computationally predicted equilibrium phases for the particulate's composition. However, the measured stoichiometries were not an exact match; rather, the Mg:Si-type phase, for example, maintained a non-equilibrium crystal structure.

3. As was just stated, the composition from XEDS of the Fe-containing phases does not perfectly correlate with the stoichiometry predicted by the thermodynamic models. Additional analysis of the Mg_2Si phase revealed a 2:1 Mg:Si stoichiometry without the equilibrium Mg_2Si crystal structure. One can explain this slight stoichiometric deviation by way of considering the fact that the phases present in the gas-atomized powder are likely meta-stable versions of the phases formed by the rapid cooling rate. This attested to the need for kinetic, time-dependent, computational analysis or non-equilibrium solidification-based thermodynamic models too.

4. Based upon concluding first three concluding items just presented and the need for kinetic computational analysis for successful modeling stage integrations in the TPM framework for cold spray already discussed, CCT curves for the formation of equilibrium Mg_2Si in the present Al 6061 system was considered for various cooling rates using JMatPro. The CCT curves were consistent with the STEM observed metastable, non-equilibrium forms of Mg_2Si identified, since the CCT curves suggest that equilibrium Mg_2Si would not form upon direct cooling given the rapid cooling rate conditions.

5. Solidification cooling rate calculations were compared with experimentally measured microstructural grain sizes using etched as-atomized particulates. Fair agreement between the experimentally inferred cooling rates and predicted

Sousa et al. Int J Metall Met Phys 2020, 5:061

ISSN: 2631-5076 |• Page 15 of 17 •

cooling rates was observed. Dendritic-solidification inspired cooling rate computational models was found to be consistent with the experimental findings, suggesting that dendritic solidification holds for gas-atomized Al 6061.

With the concluding remarks in mind, future work will further verify the experimental substation of the computational thermodynamic, kinetic and solidification modeling presented herein for cold sprayable, rapidly solidified, and gas-atomized powders in general. In the shorter term, future work will consider the use of non-equilibrium Scheil-Gulliver computational analysis of the Al 6061 composition measured herein. This will then be compared with the equilibrium phases predicted herein. Further work concerned with kinetic computational modeling will also be considered. Consideration will also be given to the incorporation of the effects of undercooling into the computational approaches taken throughout the course of this research.

Future work will also center upon the integration of the experimentally substantiated and further verified Powder Production stage of the cold spray processing based TPM with the Powder Preparation, Cold Spray Parameters, Particle Impact and Post-processing Stages too. At the same time, experimental comparison of the measured effective microstructural grain sizes from the externally etched as-atomized particulate micrographs and the cross-sectionally prepared and etched gas-atomized particulate micrographs. Electron backscatter diffraction of cross-sectionally prepared gas-atomized powder particles will also be compared with the aforementioned approaches. Finally, analysis and inspection of the additive yield strength modeling terms beyond that of the microstructurally mediated contribution will be explored.
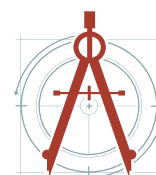
Acknowledgements

References

1. Champagne VK (2007) The cold spray materials deposition process: Fundamentals and applications. Woodhead Publishing Limited, Fl, Boca Raton, USA.

2. Sousa BC, Gleason MA, Haddad B, Champagne VK, Nardi AT, et al. (2020) Nanomechanical characterization for cold spray: From feedstock to consolidated material properties. Metals 10: 1195.

3. Sundberg K, Sousa BC, Schreiber J, Walde CE, Eden TJ, et al. (2020) Finite element modeling of single-particle impacts for the optimization of antimicrobial copper cold spray coatings. J Therm Spray Technol.

4. Sousa BC, Sundberg KL, Gleason MA, Cote DL (2020) Understanding the antipathogenic performance of nanostructured and conventional copper cold spray material consolidations and coated surfaces. Crystals 10: 504.

5. Assadi H, Schmidt T, Richter H, Kliemann JO, Binder K, et al. (2011) On parameter selection in cold spraying. J Therm Spray Technol 20: 1161-1176.

6. Nastic A, MacDonald D, Jodoin B (2020) The influence of feedstock powder. Cold Spray in the Realm of Additive Manufacturing, 33-85.

7. Tiamiyu AA, Sun Y, Nelson KA, Schuh CA (2020) Site-specific study of jetting, bonding, and local deformation during high-velocity metallic microparticle impact. Acta Mater.

8. Dykhuizen RC, Smith MF (1998) Gas dynamic principles of cold spray. Journal of Thermal Spray Technology 7: 205-212.

9. Irissou E, Legoux JG, Ryabinin AN, Jodoin B, Moreau C (2008) Review on cold spray process and technology: Part I-Intellectual property. Journal of Thermal Spray Technology 17: 495-516.

10. Stoltenhoff T, Kreye H, Richter HJ (2002) An analysis of the cold spray process and its coatings. Journal of Thermal Spray Technology 11: 542-550.

11. Champagne VK, Leyman PF, Helfritch DJ (2008) Magnesium repair by cold spray. Plating and Surface Finishing 95: 34.

12. Champagne V, Helfritch D (2016) The unique abilities of cold spray deposition. Int Mater Rev 61: 437-455.

13. Belsito D, Mcnally B, Bassett L, Champagne VK, Sisson RD (2013) Through-process modeling for cold spray alloy optimization. Proceedings MS&T.

Sousa et al. Int J Metall Met Phys 2020, 5:061

ISSN: 2631-5076 |● Page 16 of 17 ●

14. Allison J, Collins P, Spanos G (2011) From processing to properties: Through-process modeling of aluminum sheet fabrication. In: Proceedings of the 1st world congress on Integrated Computational Materials Engineering (ICME). John Wiley & Sons, Inc, Hoboken, NJ, USA, 9-17.

15. Crumbach M, Goerdeler M, Gottstein G, Neumann L, Aretz H, et al. (2004) Through- process texture modelling of aluminium alloys. Modelling and Simulation in Materials Science and Engineering 12: S1-S18.

16. Engler O, Lochte L, Hirsch J (2007) Through-process simulation of texture and properties during the thermomechanical processing of aluminium sheets. Acta Materialia 55: 5449-5463.

17. Dørum C, Laukli HI, Hopperstad OS (2009) Through-process numerical simulations of the structural behaviour of Al-Si die-castings. Computational Materials Science 46: 100-111.

18. Champagne VK, Helfritch DJ, Dinavahi SPG, Leyman PF (2011) Theoretical and experimental particle velocity in cold spray. Journal of Thermal Spray Technology 20: 425-431.

19. Zheng BL, Lin YJ, Zhou YZ, Lavernia EJ (2009) Gas atomization of amorphous aluminum: Part I. Thermal behavior calculations. Metallurgical and Materials Transactions B 40: 768-778.

20. Zheng BL, Lin YJ, Zhou YZ, Lavernia EJ (2009) Gas atomization of amorphous aluminum powder: Part II. Experimental investigation. Metallurgical and Materials Transactions B 40: 995-1004.

21. Su YH, Tsao CYA (1997) Modeling of solidification of molten metal droplet during atomization. Metallurgical and Materials Transactions B 28: 1249-1255.

22. Tsaknopoulos D (2019) Optimization of coupled computational modeling and experimentation for metallic systems: Systematic microstructural feature - mechanical property correlation for cold-sprayable powders. Worcester Polytechnic Institute.

23. Thangaraju S, Heilmaier M, Murty BS, Vadlamani SS (2012) On the estimation of true hall-petch constants and their role on the superposition law exponent in Al alloys. Adv Eng Mater 14: 892-897.

24. Boettinger WJ, Bendersky L, Early JG (1986) An analysis of the microstructure of rapidly solidified Al-8 Wt Pct Fe Powder. Metallurgical Transactions A 17: 781-790.

25. Sakaguchi Y, Harada T, Kuji T (1994) Microstructural studies of Nd-Fe-B powders produced by gas atomization. Materials Science and Engineering: A 181-182: 1232-1236.

26. He SW, Liu Y, Guo S (2009) Cooling rate calculation of non-equilibrium aluminum alloy powders prepared by gas atomization. Rare Metal Materials and Engineering 38: 353-356.

27. Sousa BC, Walde C, Champagne VK Jr, Nardi AT, Sisson RD Jr, et al. (2020) Rapidly solidified gas-atomized aluminum alloys compared with conventionally cast counterparts: Implications for cold spray materials consolidation. Coatings 10: 1035.

28. Baricco M, Bosco E, Olivetti E, Palumbo M, Rizzi P, et al. (2004) Rapid solidification of alloys. International Journal of Materials & Product Technology 20: 358-376.

29. Saunders N (2004) The modelling of stable and metastable phase formation in multi-component al-alloys. Proceedings of the 9th International Conference on Aluminium Alloys, 96-106.

30. Yu J, Li X (2011) Modelling of the precipitated phases and properties of Al-Zn-Mg-Cu alloys. Journal of Phase Equilibria and Diffusion 32: 350-360.

31. Tsaknopoulos K, Walde C, Champagne V, Cote D (2019) Gas-atomized Al 6061 powder: Phase identification and evolution during thermal treatment. JOM: The Journal of the Minerals, Metals & Materials 71: 435-443.

32. Pettersson T (2015) Characterization of metal powders produced by two gas atomizing methods for thermal spraying applications. KTH Royal Institute of Technology.

33. Rokni MR, Widener CA, Champagne VR (2014) Microstructural evolution of 6061 aluminum gas-atomized powder and high-pressure cold-sprayed deposition. J Therm Spray Technol 23: 514-524.

34. Sabard A, Hussain T (2019) Inter-particle bonding in cold spray deposition of a gas-atomised and a solution heat-treated Al 6061 powder. J Mater Sci 54: 12061-12078.

35. Tsaknopoulos K, Walde C, Tsaknopoulos D, Champagne V, Cote D (2020) Characterization of thermally treated gas-atomized Al 5056 powder. Materials 13: 4051.

36. Walde C, Tsaknopoulos K, Champagne V, Cote D (2019) The microstructural evolution of rapidly solidified powder aluminum 2024 during thermal processing. Metallogr Microstruct Anal 8: 415-425.

37. Walde C, Tsaknopoulos K, Champagne V, Cote D (2020) Phase transformations in thermally treated gas-atomized Al 7075 powder. Metallogr Microstruct Anal 9: 419-427.

38. Evans WC, Dan X, Houshmand A, Müftü S, Ando T (2019) Microstructural characterization of aluminum 6061 splats cold spray deposited on aluminum 6061-T6 substrate. Metall Mater Trans A 50: 3937-3948.

39. Bedard BA, Flanagan TJ, Ernst AT, Nardi A, Dongare AM, et al. (2018) Microstructure and micromechanical response in gas-atomized Al 6061 alloy powder and cold-sprayed splats. J Therm Spray Technol 27: 1563-1578.

40. Vijayan S, Bedard BA, Gleason MA, Leonard HR, Cote DL, et al. (2019) Studies of thermally activated processes in gas-atomized Al alloy powders: In situ STEM heating experiments on FIB-cut cross sections. J Mater Sci 54: 9921-9932.

41. Ernst AT, Kerns P, Nardi A, Brody HD, Dongare AM, et al. (2020) Surface states of gas-atomized Al 6061 powders-Effects of heat treatment. Appl Surf Sci 534: 147643.

42. Leazer JD (2015) Processing-microstructure-property relationships for cold spray powder deposition of Al-Cu alloys. Naval Postgraduate School.

43. Duflos F, Stohr JF (1982) Comparison of the quench rates attained in gas-atomized powders and melt-spun ribbons of Co- and Ni-base superalloys: Influence on resulting microstructures. J Mater Sci 17: 3641-3652.

44. Martín A, Cepeda-Jiménez CM, Pérez-Prado MT (2020) Gas atomization of γ -TiAl alloy powder for additive manufacturing. Adv Eng Mater 22: 1900594.